Plane waves and structures in turbulent channel flow

L. Sirovich
Center for Fluid Mechanics, Turbulence and Computation and Division of Applied Mathematics, Brown University, Providence, Rhode Island 02912

K. S. Ball
Department of Mechanical Engineering, The University of Texas at Austin, Austin, Texas 78712

L. R. Keefe
Center for Turbulence Research, NASA–Ames Research Center, Moffett Field, California 94035

(Received 20 February 1990; accepted 31 July 1990)

A direct simulation of turbulent flow in a channel is analyzed by the method of empirical eigenfunctions (Karhunen–Loève procedure, proper orthogonal decomposition). This analysis reveals the presence of propagating plane waves in the turbulent flow. The velocity of propagation is determined by the flow velocity at the location of maximal Reynolds stress. The analysis further suggests that the interaction of these waves appears to be essential to the local production of turbulence via *bursting* or *sweeping* events in the turbulent boundary layer, with the additional suggestion that the *fast acting* plane waves act as *triggers*.

I. INTRODUCTION

In an early paper Betchov[1] suggested that the transition process in wall bounded flows is due to secondary instability. The essential three-dimensionality of this transition process was experimentally demonstrated by Klebanoff *et al.*[2] An important qualitative analysis of this behavior, based on kinematical wave theory, is to be found in the work of Landahl,[3] and a detailed picture of the instability mechanisms at work in boundary layer and parallel flows has been presented by Orszag and Patera[4–6] and Herbert.[7,8] Recent reviews of this work have been given by Herbert[9] and Bayley *et al.*[10] In brief, the present picture of the phenomena holds that instabilities secondary to the two-dimensional Tollmien–Schlichting (T–S) waves traveling obliquely to the streamwise direction cause the unsettling of the flow. (These analyses furnish a critical Reynolds number, Re, which more nearly corresponds to experiment.) Thus plane waves traveling at an angle to the propagation vector of the T–S waves, and which ride *piggyback* on these, experience the greatest growth.

In the present study we show that plane wave modes are present in turbulent flows and continue to play an important if not essential role in turbulent wall bounded flows. The case which we treat is that of plane channel flow (Poiseuille flow) at $\mathrm{Re} = 1500$ (based on the channel half-width δ) or equivalently $\mathrm{Re}_\tau = 80$, based on the wall shear velocity u_τ. This is the flow generated numerically by Keefe *et al.*[11] for the study of Lyapunov dimension and analyzed by the proper orthogonal decomposition[12,13] by Ball *et al.*[14] The dimensions of the computational cell, based on channel half-width, are $1.6\pi \times 2 \times 1.6\pi$ (in x,y,z—the streamwise, normal, and spanwise directions), with a corresponding grid resolution of $24 \times 33 \times 12$. This is somewhat on the coarse side but adequate for present purposes. Henningson *et al.*,[15] in their study of the growth of a turbulent spot, consider the same Re and a cell size $35\pi \times 2 \times 25\pi$ with a resolution of $256 \times 33 \times 256$. Thus they have a similar coarse graining but pay more attention to large scales. As a result of the disregard of large scales and thus fewer memory demands we are able to observe the overall flow at relatively fine time increments. This is of some importance in the analysis that follows. (See Ref. 14 for more details of our simulation.)

The Reynolds number for the flow under consideration, $\mathrm{Re} = 1500$, is perhaps only 15% above the critical Re based on numerical experiments.[4–6] In the terminology of Patel and Head[16] the turbulence is *continuous* but not *fully developed*. Unlike the case for closed flows, Keefe *et al.*[11] have shown that the attractor size of channel flow grows *explosively* and that the Hausdorf dimension is roughly 780 at this value of Re. Therefore, relatively many modes participate in the detailed motion of the flow. The structures represented by these modes and their importance in the dynamical behavior of turbulent channel flow is presented in the next section.

II. PRELIMINARY DISCUSSION

The numerically generated flow under consideration is driven by a fixed pressure gradient. As a result, in the chaotic regime the flow rate Q changes with time. This flow rate can be thought of as undergoing a *chugging* motion. At the initial instant the flow is essentially laminar (Poiseuillian). The corresponding flow rate exceeds the mean turbulent value preferred by the flow and is therefore an unstable rate for Q. Instability first and then chaos act to diminish this flow rate. When the flow rate falls below the critical flow rate the flow then tends to relaminarize. In the process the flow rate exceeds its critical value again (before becoming Poiseuillian) and the process repeats. In this respect the phenomenon resembles what is found in pipe flow as first noted by Reynolds.[17] (A difference, however, is that the turbulence here can establish itself laterally and spread.) Thus the flow undergoes uneven cycles of *contraction* and *expansion*. In most flow experiments the mass flow rate is controlled,[18–21] and the intermittency then appears in the pressure drop. Figure 1 shows a segment of the time history of the flow rate obtained in this simulation (as indicated by the bulk mean velocity through the channel, u_m). Furthermore, this process can be regarded as taking place locally but in extended regions of

 0899-8213/90/122217-10$02.00

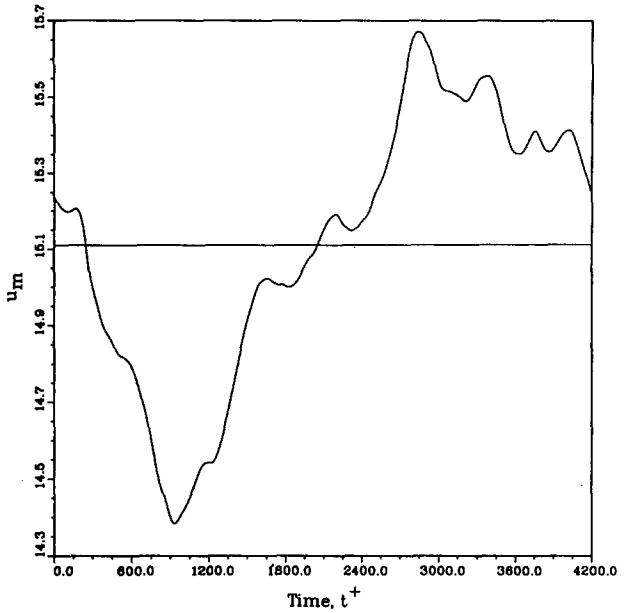

FIG. 1. Variations in bulk mean velocity, $u_m(t^+)$.

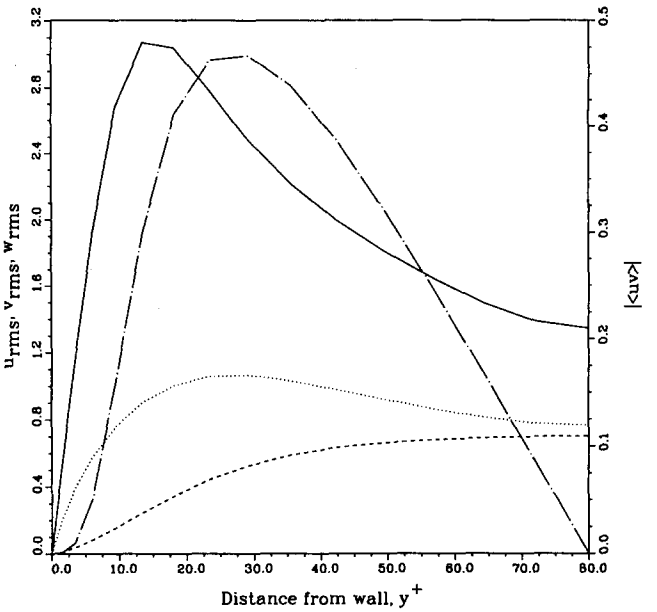

FIG. 2. Root-mean-square velocity fluctuations and Reynolds shear stress across the channel: ——, u_{rms}; ---, v_{rms}; ···, w_{rms}; —·—, $|\langle uv \rangle|$.

space. Only some regions of the flow are in the process of becoming turbulent while other regions are in the process of relaminarizing. The process just described bears a relationship to the growth of turbulent spots[22,23] and the results that are presented here bear on the recent numerical study of spot spread by Henningson[24] based on kinematical wave theory. As will be seen our results show some resemblance to critical layer phenomena in linear stability theory. By contrast the recent experiments and analysis of Kistler and Markus[25] appear to minimize the role of the critical layer in the acceleration of retarded spots. However, since they did not produce *bursts* this point requires further study.

A characteristic feature of the destabilizing effect on the flow being described is the phenomenon of turbulence-producing events, viz., *bursts* and *sweeps* as described by Willmarth.[26,27] These events are main contributors to the Reynolds shear stress, as has been well established in both experiment[28] and computation.[29] As preparation for describing these we show in Fig. 2 the distribution of the rms velocity fluctuations and the mean Reynolds shear stress across the channel. The center of the channel is at $y^+ = 80.0$ (in wall units), and the ensemble-averaged flow is symmetric about the midplane.

It is observed that for this low Reynolds number flow, the maximum Reynolds shear stress occurs near the plane $y^+ = 30$. Kim *et al.*[29] also find a peak Reynolds stress in the same vicinity at the higher value Re = 3300. (Here, as in Ref. 29, the peak rms value of u lies near $y^+ = 15$.) This agrees with the experiments of Eckelmann.[30] At higher Reynolds numbers the location of peak Reynolds stress moves farther away from the wall.[31] (We mention in passing that a linear stability analysis of laminar flow at the same value of Re leads to a peak velocity perturbation at $y^+ \approx 14$ and a peak Reynolds stress at $y^+ \approx 26$ for the most unstable mode. However, if the turbulent mean velocity profile is used in the stability analysis both peaks occur at different locations, relatively near the centerline.[32]) There is both theoretical[33] and experimental[34] evidence that y^+ is of order $(\sqrt{\mathrm{Re}_\tau})$, where Re_τ is the Reynolds number based on friction velocity. Sreenivasan[34] also finds that peak u_{rms} occurs at $y^+ = 15$ over a wide range of Re_τ. The latter is in keeping with universal wall behavior which leads to the log layer but the location of peak Reynolds stress obviously does not follow this scaling. Townsend[35] has pointed out that not all of the wall dynamics follow the *universal* scaling and invokes the notion of "active and inactive motions" (see also Bradshaw[36]) to account for the differences. Our understanding of this region is incomplete.

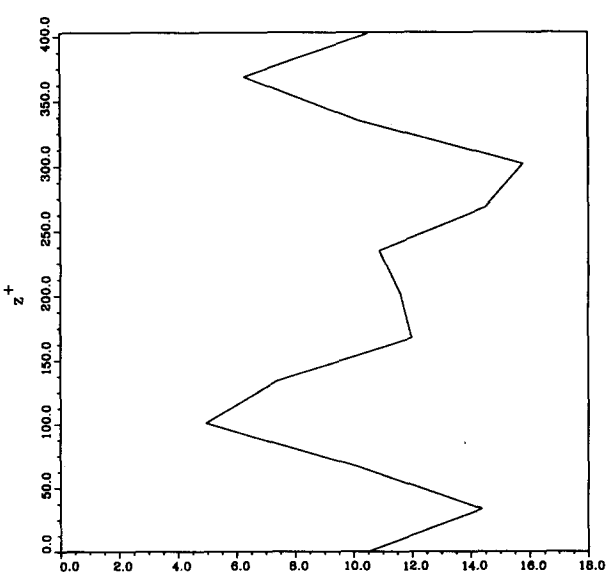

FIG. 3. Velocity profile, u, at $y^+ = 13.48$ at fixed values of x and t.

The existence of wall-layer streaks[37] in the present simulation is indicated by Fig. 3, which displays an instantaneous streamwise velocity profile in the spanwise direction at a fixed value of x^+. The streak spacing approaches the accepted value $\lambda_z^+ \approx 100$ when averaging is done over the entire ensemble. As noted by Kim *et al.*,[29] wall-layer streaks are consistent with the existence of streamwise vortical structures.

The passage of local turbulence-producing events (Reynolds shear stress) is depicted in Fig. 4, which shows the plane $y^+ = 29.25$ at the sequence of times indicated. Solid contours indicate $-uv > 0$ for $v > 0$ (bursts) and dashed contours indicate $-uv > 0$ for $v < 0$ (sweeps). [Since the numerical simulation assumes periodicity in the streamwise (and spanwise) direction the structures reenter at the left after leaving at the right.] As has been previously observed,[38] in fully developed turbulent flows these local structures travel downstream throughout the near-wall region. In the buffer layer at $y^+ = 15$, Johansson *et al.*[38] report this velocity to be about $10.6u_\tau$, which corresponds to the local mean velocity at that elevation. For the flow under consideration here, the waves produce structures that are *advected* with the mean velocity at the plane of peak Reynolds shear stress, namely $u(y^+ = 30) \approx 15.8u_\tau$. As will be seen in Sec. IV the maximal disturbance region lies in the vicinity of maximal Reynolds stress.

To analyze the flow we have found it useful to use the Karhunen–Loève procedure for generating empirical eigenfunctions (also referred to as proper orthogonal decomposition by Lumley[12,13]). This method has received a number of

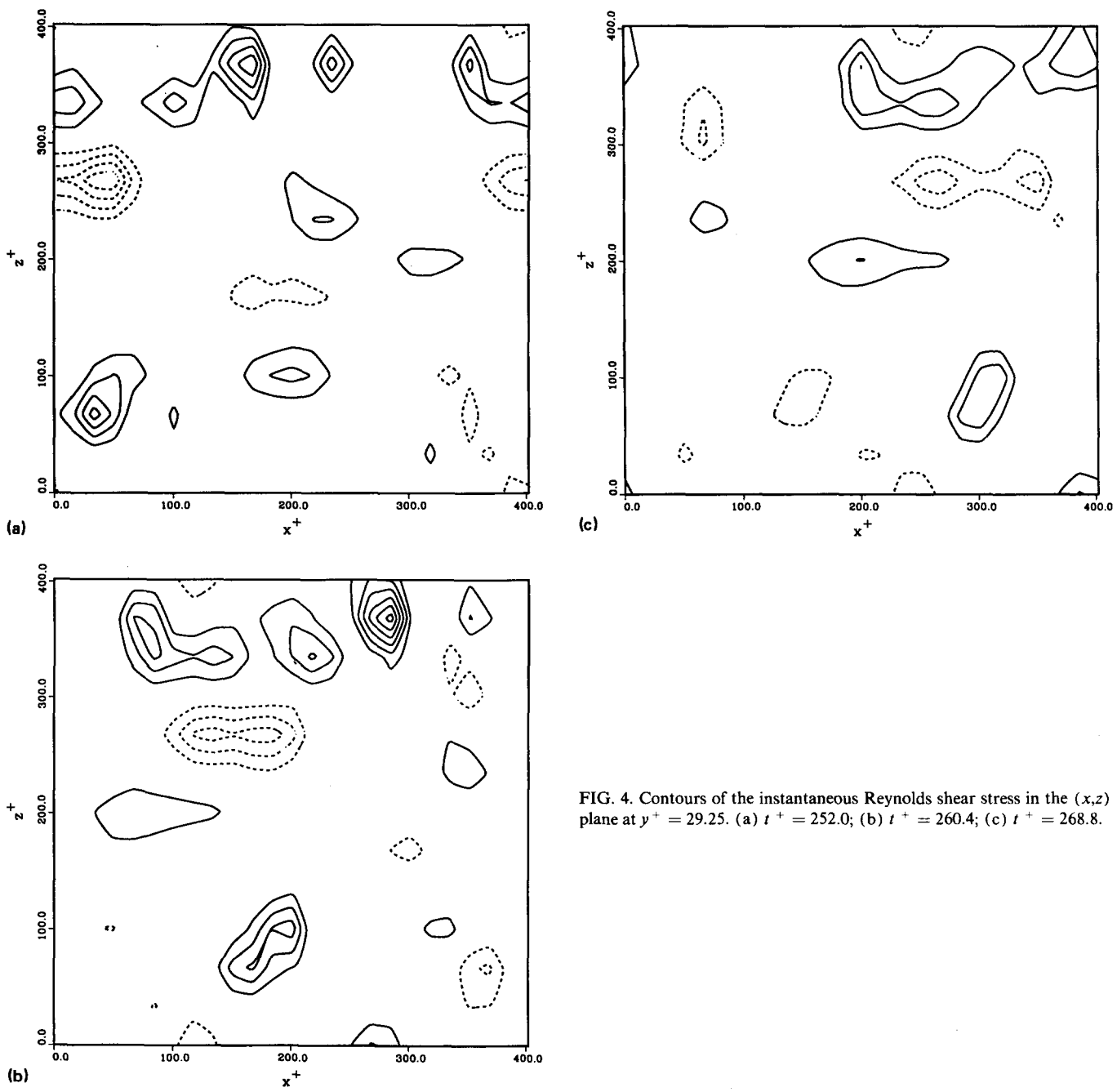

FIG. 4. Contours of the instantaneous Reynolds shear stress in the (x,z) plane at $y^+ = 29.25$. (a) $t^+ = 252.0$; (b) $t^+ = 260.4$; (c) $t^+ = 268.8$.

extensions for use in fluid flows and is well described in the literature.[39–43] In brief, the procedure entails forming the correlation matrix

$$K_{ij}(\mathbf{x},\mathbf{x}') = \langle u_i(\mathbf{x}) u_j(\mathbf{x}') \rangle, \tag{1}$$

where angle brackets indicate an ensemble average. The empirical eigenfunctions (which in a well-defined sense are the optimal functions for describing the flow) are obtained by solving the integral equation

$$\int K_{ij}(\mathbf{x},\mathbf{x}') V_j(\mathbf{x}') d\mathbf{x}' = \lambda V_i(\mathbf{x}) \tag{2}$$

(summation convention assumed) where integration is over the domain of the flow. (This is finite in the present instance as a result of the spatial periodicity of the simulation.) On mathematical grounds the eigenfunctions can be taken to be a complete orthonormal basis set. If the complex inner product

$$(\mathbf{f},\mathbf{g}) = \int f_j^*(\mathbf{x}) g_j(\mathbf{x}) d\mathbf{x} \tag{3}$$

is defined (the asterisk denotes the complex conjugate), then

$$\lambda = \langle (\mathbf{V},\mathbf{u})^2 \rangle \tag{4}$$

is seen to give the average *energy* of the flow in the **V** direction, and if **W** and **V** represent two different empirical eigenfunctions then

$$\langle (\mathbf{W},\mathbf{u})(\mathbf{V},\mathbf{u}) \rangle = 0, \tag{5}$$

which shows that the various modes are statistically orthogonal or uncorrelated. Since ensemble averages can be regarded as being time averages, this also states that the modes are uncorrelated in time. *It is important for later discussion to understand that this does not imply that the modes do not participate in important short time interaction.*

III. PLANE WAVE MODES

As a result of the fact that the flow is unbounded in the x and z directions, K_{ij} is homogeneous in those directions[39] and the eigenfunctions take on the form

$$U_k^{(q)}(x,y,z) = V^{(q)}(y;\mathbf{k}) e^{-i(k_1 x + k_3 z)}$$
$$= V_{\mathbf{k}}^{(q)}(y) \exp(-i\mathbf{k}\cdot\mathbf{x}), \tag{6}$$

where $\mathbf{k} = (k_1,0,k_3)$. The superscript or quantum number q reflects the fact that for each $\mathbf{k}$ there is a hierarchy of modes. Thus the empirical eigenfunctions can naturally be regarded as *plane waves*. In the simulation both streamwise and spanwise directions are taken to be periodic. Thus we write

$$k_1 = 2\pi m/L_x, \quad k_3 = 2\pi n/L_z, \tag{7}$$

where L_x and L_z represent the length scales in the streamwise and spanwise directions. For later reference it is useful to measure L_x and L_z in wall units. Since the half-channel height is 80 wall units it follows that

$$L_x^+ = L_z^+ \approx 400, \tag{8}$$

where the $+$ superscripts denote wall units. In any case the integers m and n of (7) denote the number of full waves in each of the two directions.

As a word of caution we point out that the presence of Fourier modes in the x and z directions in no way implies linear behavior. For example, the interaction of modes $\mathbf{V}_{\mathbf{k}}^{(q)}$ and $\mathbf{V}_{\mathbf{k}'}^{(q')}$ will produce a *wave* of wave number $\mathbf{k}+\mathbf{k}'$. However from (5) it follows that these modes will be *statistically orthogonal* if $\mathbf{k}+\mathbf{k}' \neq 0$. In rough terms one might say that independent modes interact on a short time scale but not on a long time scale.

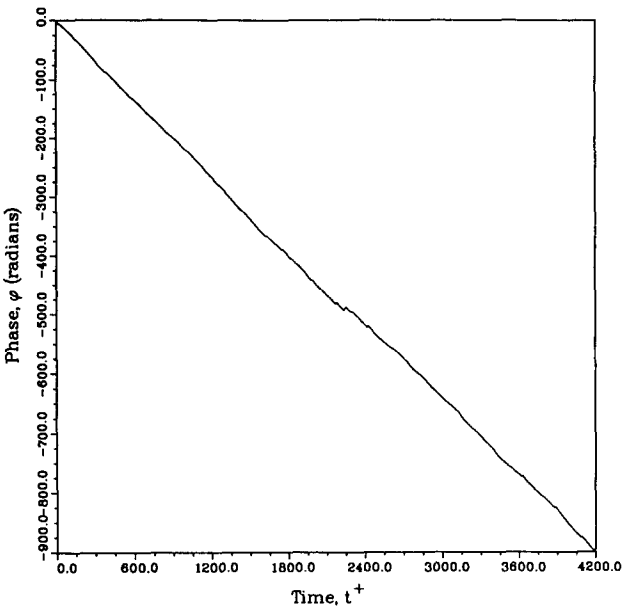

FIG. 5. The time history of the phase for the eigenfunction with $\mathbf{k} = (1,3,1)$.

The projection of the flow along an eigenfunction

$$a_{\mathbf{k}}^{(q)}(t) = (\mathbf{V}_{\mathbf{k}}^{(q)},\mathbf{u}) \tag{9}$$

furnishes a time history of the mode, which itself is the eigenfunction of the temporal snapshot kernel.[39] For example, in Fig. 5 we plot the history of the phase of $a_{13}^{(1)}(t)$. The phase is defined by

$$\phi_{13}^{(1)} = \tan^{-1}[\mathrm{Im}(a_{13}^{(1)})/\mathrm{Re}(a_{13}^{(1)})]. \tag{10}$$

It is clear that this mode has a secular time course described by a single frequency,

$$\omega_{13}^{(1)} = \lim_{t\uparrow\infty} \phi_{13}^{(1)}/t. \tag{11}$$

Thus if we represent the actual flow in terms of the empirical eigenfunctions

$$\mathbf{u} = \sum_{q,\mathbf{k}} a_{\mathbf{k}}^{(q)}(t) \mathbf{V}_{\mathbf{k}}^{(q)} = \sum_{q,\mathbf{k}} \mathbf{v}_{\mathbf{k}}^{(q)}, \tag{12}$$

then, in particular, $\mathbf{v}_{13}^{(1)}$ has the form

$$\mathbf{v}_{13}^{(1)} = b_{13}^{(1)}(t) V_{13}^{(1)}(y) e^{i(\omega_{13}^{(1)} t - \mathbf{k}\cdot\mathbf{x})} \tag{13}$$

of a propagating plane wave with direction determined by $m=1$ and $n=3$ [see (7)]. The time-dependent coefficient or magnitude, $b_{13}^{(1)}(t)$, is typical of variables found in turbulent flows and its magnitude is shown in Fig. 6.

Before elaborating on this result we pause to define the energy of the flow,

$$E = \langle (\mathbf{u},\mathbf{u}) \rangle = \sum_{q,\mathbf{k}} \lambda_{\mathbf{k}}^{(q)}. \tag{14}$$

A list of eigenvalues is shown in Table I. If we choose as a

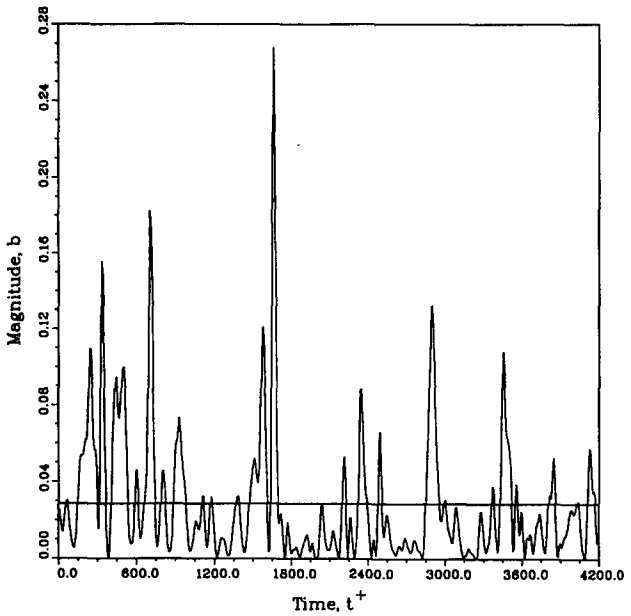

FIG. 6. The time history of the magnitude for the eigenfunction with $\mathbf{k} = (1,3,1)$. The horizontal line is the eigenvalue for this mode.

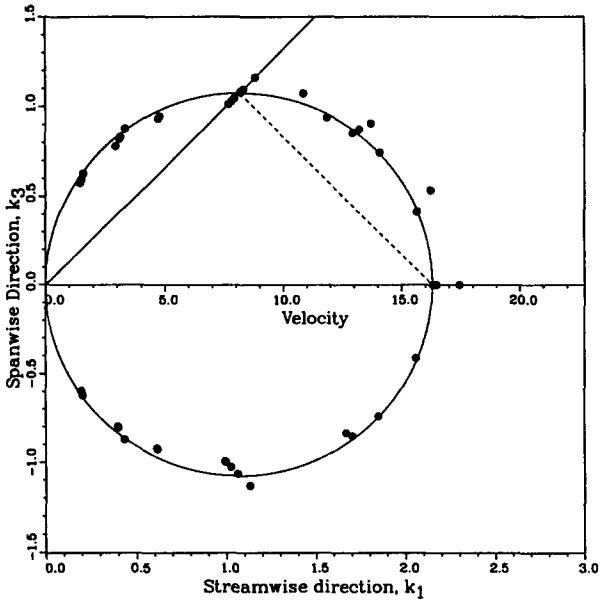

FIG. 7. Normal speed locus.

TABLE I. A summary of the eigenvalue calculation: First 38 values.

Index	m	n	q	Eigenvalue	Degeneracy	Energy, fraction of total
1	0	1	1	0.226 71	2	0.1300
2	0	2	1	0.152 34	2	0.0874
3	0	3	1	0.127 74	2	0.0732
4	0	2	2	0.120 77	2	0.0693
5	0	1	2	0.073 83	2	0.0423
6	0	3	2	0.071 25	2	0.0408
7	1	3	1	0.028 57	4	0.0327
8	0	0	1	0.106 63	1	0.0305
9	1	3	2	0.023 24	4	0.0266
10	0	1	3	0.032 79	2	0.0188
11	1	2	1	0.013 67	4	0.0156
12	0	0	2	0.051 41	1	0.0147
13	1	2	2	0.011 95	4	0.0137
14	0	1	4	0.021 11	2	0.0121
15	0	2	3	0.020 95	2	0.0120
16	1	1	1	0.009 32	4	0.0107
17	1	1	2	0.009 07	4	0.0104
18	1	2	3	0.007 10	4	0.0081
19	0	0	3	0.027 83	1	0.0079
20	1	3	3	0.006 70	4	0.0076
21	1	3	4	0.006 30	4	0.0072
22	2	3	1	0.006 20	4	0.0071
23	1	1	3	0.006 09	4	0.0069
24	0	3	3	0.012 04	2	0.0069
25	0	3	4	0.011 73	2	0.0067
26	2	3	2	0.005 51	4	0.0063
27	1	2	4	0.005 34	4	0.0061
28	2	2	1	0.005 08	4	0.0058
29	0	2	4	0.009 61	2	0.0055
30	0	0	4	0.018 76	1	0.0054
31	2	2	2	0.004 10	4	0.0047
32	2	1	1	0.004 06	4	0.0047
33	0	0	5	0.016 20	1	0.0046
34	0	1	5	0.007 56	2	0.0043
35	0	1	6	0.007 28	2	0.0042
36	1	1	4	0.003 53	4	0.0040
37	1	0	1	0.006 83	2	0.0039
38	2	1	2	0.003 29	4	0.0038

criterion of mode significance that $\lambda_k^{(q)}/E > 10^{-2}$, then we have determined from the simulation that for all significant modes

$$\omega_{k_1 k_3}^{(q)} \neq 0, \quad k_1 \neq 0 \tag{15a}$$

and

$$\omega_{0,k_3}^{(q)} = 0. \tag{15b}$$

Thus all modes corresponding to zero wave number in the streamwise direction are nonpropagating modes and we term these *kinematically degenerate*. We do this since it is our contention that the $k_1 = 0$ modes are, to a large degree, a result of the finite grid. Clearly such modes show no variation in the streamwise direction and therefore imply a strong (infinite) correlation in this direction (periodicity confers a false correlation in the streamwise direction, but the issue at hand is different from this). These modes appear because the mesh is not able to resolve slightly off streamwise directions and therefore places energy in the $k_1 = 0$ modes. From the well-known streakiness of the flow[37] we know that there is considerable energy in the slightly off streamwise directions and we can presume that as a result of the finite mesh these appear as $k_1 = 0$ modes. A study of Table I shows that the kinematically degenerate modes carry the overwhelming majority of the fluctuation energy of the flow.

The possible relationship of the propagating waves to the structures described earlier is clearly of interest. To develop this idea further we first consider the normal speeds of the waves

$$c_{\mathbf{k}} = \omega/|\mathbf{k}|. \tag{16}$$

In Fig. 7 we plot the normal speed locus

$$\mathbf{c}_{\mathbf{k}} = (\omega/|\mathbf{k}|)\mathbf{k}, \tag{17}$$

i.e., speed (16) versus the direction $\mathbf{k}/|\mathbf{k}|$. Actually, since the results follow from a simulation only a discrete set of points (heavy dots) are shown in this polar plot. In addition only those corresponding to the most energetic modes are

indicated, viz., $(m,n) = (1,0)$, $(1,1)$, $(1,2)$, $(1,3)$ and $(2,1)$, $(2,2)$, $(2,3)$, with (7) defining the relation between $\mathbf{k}$ and (m,n).

At each point of the locus we construct the plane wave that is perpendicular to the propagation vector (17), as indicated by the dotted line in Fig. 7 for a representative point. This represents the location of the plane wave, initially located at the origin, after a unit time has elapsed. The collection of these plane waves generates an *envelope* which can be thought of as locating the most intense signal. Only the most energetic waves mentioned above have been considered in the construction. Since the normal speed locus is well approximated by a circle the envelope is simply a point. This in turn implies that these plane waves move, as indicated in Fig. 8, by displacement in the streamwise direction. This streamwise displacement is indicated by the arrows, and shows how actual wave segments of the plane wave travel. (For hyperbolic systems of partial differential equations the above construction is used to generate the characteristic surface, also called the pedal curve,[44] which in turn reveals how infinitesimal disturbances propagate.)

Consider the two wave segments shown in Fig. 8, denoted as (a) and (b). Their phase speeds are given as c_a and c_b, respectively, where c is defined by (16). After a fixed time increment, these waves travel to new positions labeled as (a') and (b'). If the two phase speeds c_a and c_b are related as shown, namely $c_b = c_a \cos\theta$, then the waves can continuously interact at a fixed spanwise location z as they travel downstream, i.e., they form an envelope that propagates in the streamwise direction. As the angle θ increases, the normal speed c_b becomes smaller for a given wave segment speed c_a. Thus the wave segment speed can be much larger than the normal speed. The geometric representation of Fig. 8 leads directly to the circular locus of Fig. 7, and the pedal curve corresponds to the wave segment speed c_a.

What has been referred to as the segment speed in the previous paragraph is to a close approximation equal to the mean flow velocity in the plane of peak Reynolds shear stress, $y^+ \approx 30$. Some basis for the underlying mechanics leading to this result is obtained by viewing the y dependence of the eigenfunction. The three components of $\mathbf{V}_{13}^{(1)}$ and $\mathbf{V}_{13}^{(2)}$, the two most energetic propagating modes, are shown in Fig. 9. [Since $\mathbf{K}(\mathbf{x},\mathbf{x}')$,(1) is Hermitian, the eigenfunctions are real, although for convenience we have used the complex representation (6).] For purposes of comparison we have also plotted the average value of the Reynolds shear stress, $\langle uv \rangle$. It is seen from these curves that the streamwise component of the eigenfunctions, which is the largest member, has its principal support in the region where $|\langle uv \rangle|$ is a maximum. There is a superficial analogy with linear stability the-

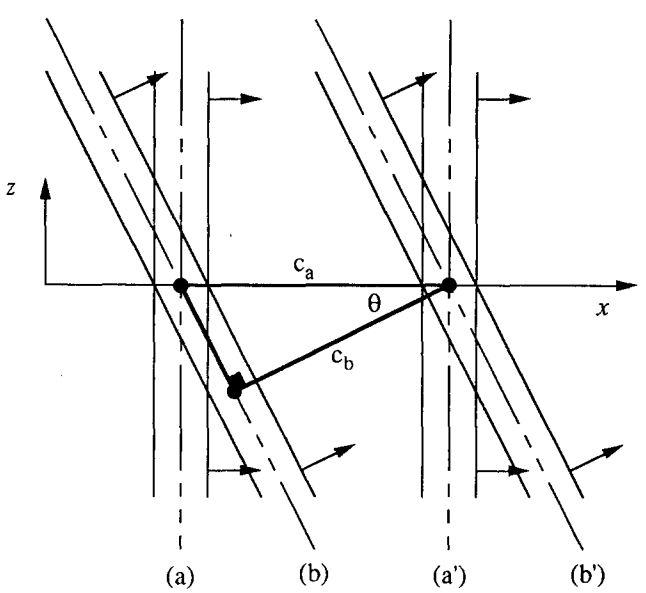

FIG. 8. Motion of plane waves.

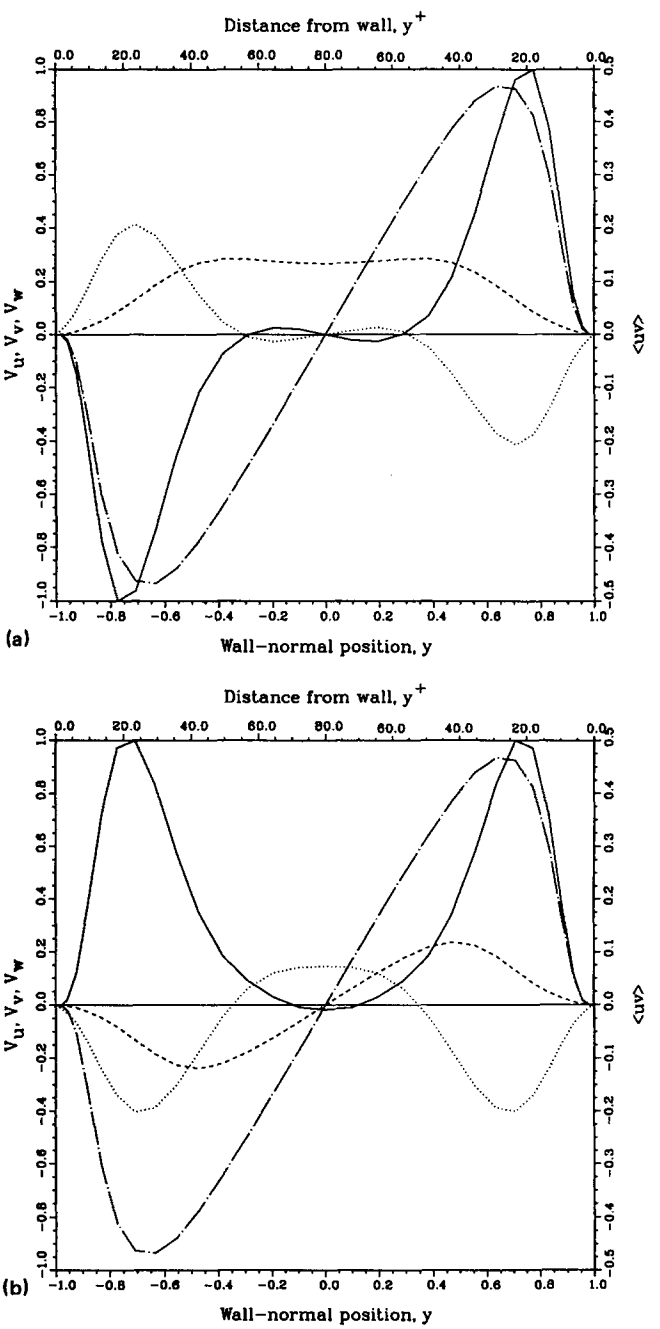

FIG. 9. (a) The spatial structure of the eigenfunction with $\mathbf{k} = (1,3,1)$:—, V_u; ---, V_v; ···, V_w; —·—, $\langle uv \rangle$. (b) The spatial structure of the eigenfunction with $\mathbf{k} = (1,3,2)$:——, V_u; ---, V_v; ···, V_w; —·—, $\langle uv \rangle$.

ory in which the maximal disturbance and its corresponding Reynolds stress bear a similar relationship (see Sec. II). However, the actual critical layer which results from a straightforward linear theory based on the mean velocity profile is well removed from the buffer region, and is roughly at $y^+ = 56$. Nevertheless, the plane waves from Fig. 9 are best able to extract energy from the mean flow via the Reynolds stress at this location, which gives some basis as to why the plane waves propagate with the mean fluid velocity at this elevation. It may be shown that the individual Chebyshev components that make up the vertical portion of the eigenfunctions also exhibit the propagation property. But such a decomposition would be a step backward, since it is the superposition of the Chebyshev modes that gives the eigenfunction property. Only as a result of this do we find that the support lies in a relatively narrow domain.

The other plane waves which have not been indicated in Fig. 7 carry little energy, as study of Table I shows. One explanation is that their speed is not that of the buffer region and a study of their vertical form[14] shows that their principal support lies elsewhere. One feature of this picture which can be regarded as puzzling is why $\lambda_{10}^{(1)}$ is as small as it is. This corresponds to a plane wave in the streamwise direction, i.e., with crests perpendicular to the streamwise direction. This wave would appear to be suited for the extraction of energy from the buffer region. To gain some understanding on why it does not, we start by pointing out that the assembly of the most energetic modes corresponds to rolls of fluid aligned with the stream. (See the characteristic eddy of construction given by Moin and Moser.[45]) A sketch of the motion is shown in Fig. 10. From Table I we see that a significant portion of the fluctuation energy lies in such roll-like motions. (Note from Table I that modes with two and three pairs of rolls have a comparable amount of energy. This is discussed further in Sec. V.) From a comparison of the velocity components for the latter with the λ_{10} mode, it would appear that a wave propagating in the streamwise direction finds it difficult to extract energy from the rolling fluctuations. Note that the λ_{10} mode has a substantial component in the streamwise direction while the rolling modes have no streamwise component. Thus the modes are mismatched. This is not true for a plane wave propagating obliquely. To see this we can transform to a coordinate system for which one axis is the direction of the wave. Then a simple resolution of velocities shows that the obliquely traveling wave can capture energy from the roll-like fluctuations since the mismatch is partially removed and they share momenta in the same direction.

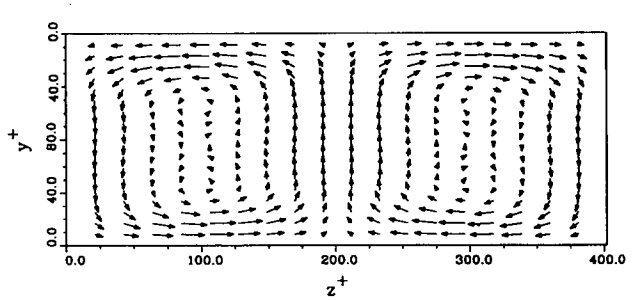

FIG. 10. Representative mode, $\mathbf{k} = (0,1,1)$, showing roll-like motion in (y,z) plane.

IV. BURSTING STRUCTURES

We next want to assess the effect of the propagating waves on the flow and, in particular, to relate this to the traveling structures discussed at the outset in regard to Fig. 4. There are three aspects of this that are worth mentioning. First as we shall see the structures are relatively energetic events. More precisely the *instantaneous* Reynolds stress uv (by which we monitor structure activity) is relatively large. Second, the energy in the propagating modes, as seen in Table I, is relatively small. Thus the propagating modes alone cannot account for the structures—but we speculate on evidence to be presented that they are part of a *triggering* mechanism. This brings up the third point which is that the propagating modes (in fact, all modes) are uncorrelated in time, see (5). Hence if the plane waves are a triggering device we must look for short term interactions.

We start by recalling the representation of the flow given by (12). The original flow field is reconstructed without approximation when the sum is over the set of all modes $\mathbf{v}_\mathbf{k}^{(q)}$. However, due to the optimal convergence of the empirical eigenfunctions, summing over a much smaller subset of $\mathbf{v}_\mathbf{k}^{(q)}$ provides us with a relatively accurate representation of the flow. We denote by

$$\mathbf{u}_N = \sum_{q,\mathbf{k}\subset\mathbf{N}} a_\mathbf{k}^{(q)} \mathbf{v}_\mathbf{k}^{(q)} \tag{18}$$

the representation of the flow in terms of the first N-most energetic modes, where $\mathbf{N}$ denotes the corresponding set of indices. For our purposes here, choosing $N = 38$ (the modes listed in Table I) will suffice. These modes contain 76% of the fluctuation energy of the flow.

We next divide these modes into two subsets, one containing the propagating modes $\mathbf{k}_p = (k_1 \neq 0,0,k_3)$ and the other containing the kinematically degenerate modes $\mathbf{k}_d = (k_1 = 0,0,k_3)$, and denote by

$$\mathbf{u}_N^P = \sum_{q,\mathbf{k}_p\in\mathbf{N}} \mathbf{v}_{\mathbf{k}_p}^{(q)} \tag{19}$$

and

$$\mathbf{u}_N^D = \sum_{q,\mathbf{k}_d\in\mathbf{N}} \mathbf{v}_{\mathbf{k}_d}^{(q)} \tag{20}$$

the *model* flows taken over the set of propagating and nonpropagating modes, respectively.

To illustrate the character of each representation given above, second quadrant occurrences of uv (burst, $uv<0$ with $v>0$) are selected over time at a typical fixed point in the flow. In Fig. 11(a), results for the full numerical simulation are presented. The passage of several bursts is observed, and the individual *ejections* of fluid comprising each burst are also evident. We again mention that the periodicity of the computational domain allows a given structure to pass the same point in the flow more than once, so that a one-to-one correspondence between each individual peak in Fig. 11 with an ejection is not to be assumed. However, the existence of individual ejections within each burst as indicated by the nested set of continuous curves is apparent.

The truncated representation of the full flow given by $\mathbf{u}_N$ is used in Fig. 11(b). Even with just 38 modes, a high

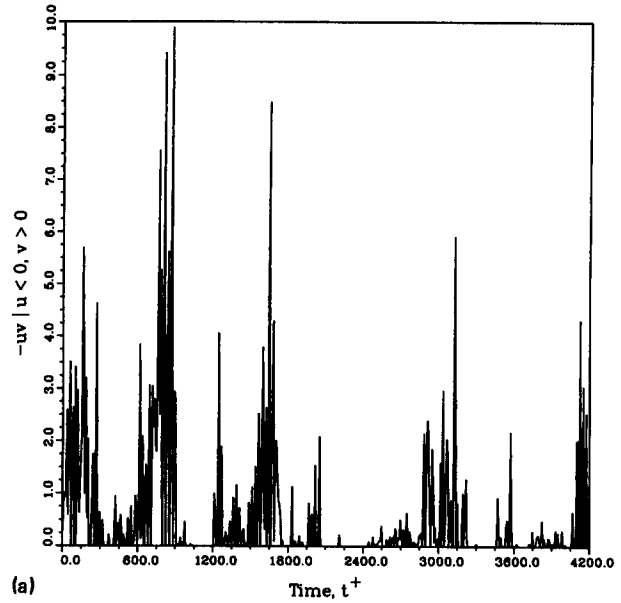

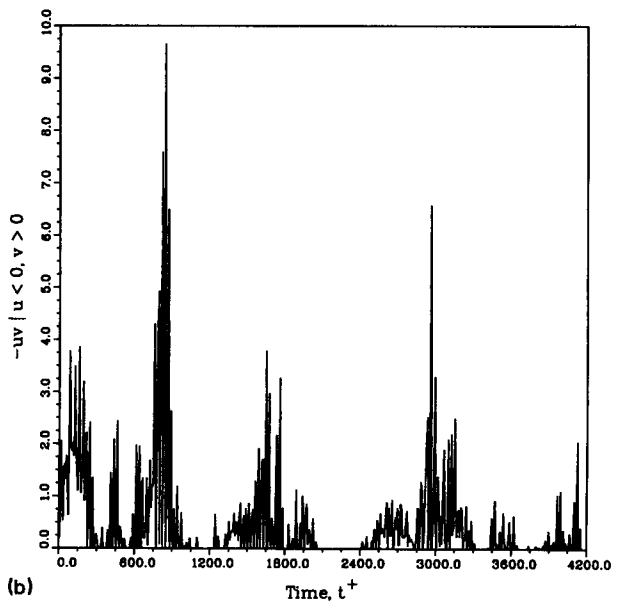

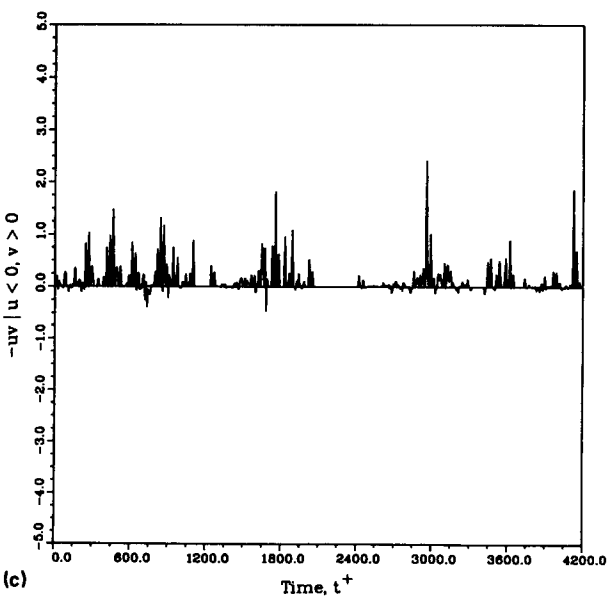

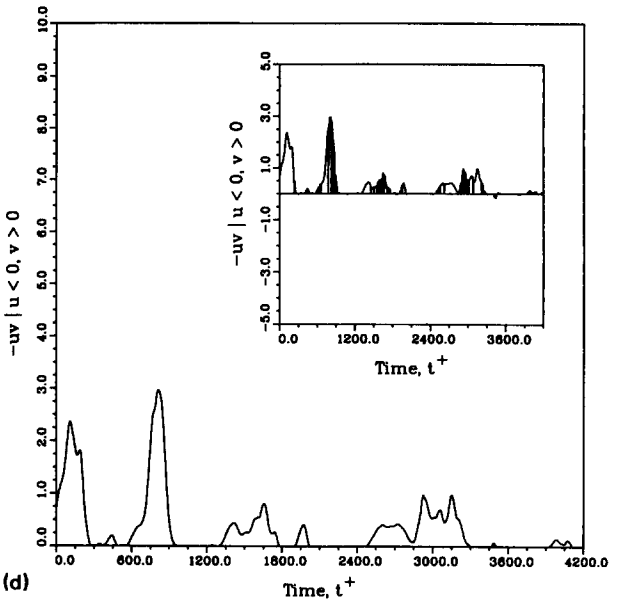

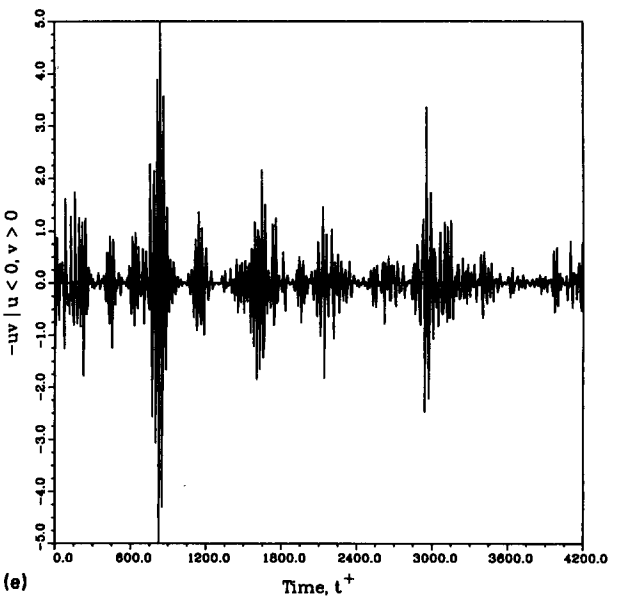

FIG. 11. Second-quadrant occurrences of the instantaneous Reynolds shear stress, uv, at a fixed point in the (x,z) plane at $y^+ = 29.25$. (a) Full numerical simulation; (b) representation of flow using first 38 modes; (c) representation of flow using propagating (fast) modes; (d) representation of flow using kinematically degenerate (slow) modes (inset shows actual curve with sampling artifact not removed); (e) representation of flow in terms of the interaction between the slow and fast modes.

degree of accuracy is obtained, with the uv signal from $\mathbf{u}_N$ correlating very well with that from the full flow.

To assess the relative effects of the propagating and kinematically degenerate modes we express the approximate instantaneous Reynolds stress by

$$u_N v_N = (u_N^D + u_N^P)(v_N^D + v_N^P)$$
$$= (u_N^P v_N^P) + (u_N^D v_N^D) + (u_N^P v_N^D + u_N^D v_N^P). \quad (21)$$

Figures (11c)–(11e) show the time evolution of the three terms in (21), respectively. We follow standard practice and view (21) for second quadrant events. As a result we conditionally sample (21) viewing it for times at which $u_N v_N < 0$ and $v_N > 0$. This fact is important in viewing Fig. 11(d), since there are downward spikes present as shown in the inset. These are artifacts introduced by the time sampling. The actual time course of the degenerate modes with this artifact removed is smooth, as shown in the main figure. By comparison with the *fast* excitation seen in Fig. 11(c) these are justifiably termed *slow* excitations.

Several features are worth remarking on. First we note that the peaks in Figs. 11(c) and 11(d) are well below those seen in Fig. 11(b). While the magnitudes of the peaks in Fig. 11(d) are somewhat higher than in Fig. 11(c), they still fall considerably short of the peak magnitudes for the full flow. Second, the curves in Figs. 11(c) and 11(d) are of a strikingly different character. The nonpropagating modes used in Fig. 11(d) produce a relatively smooth curve (when the artifactual downstrokes are removed) while the curve generated by the propagating modes is quite spiky, as in Figs. 11(a) and 11(b).

A better understanding of the bursting phenomenon follows the study of Fig. 11(e) in conjunction with the previous two figures. Clearly this figure shows the most dramatic temporal excursions. From this figure we conclude that although the energy exhibited in the fast activity of the propagating modes is relatively small in magnitude, extreme excursions will not occur without these. This is further underscored by the fact that the time course seen in Fig. 11(b) has a similar nature to that in Fig. 11(c). It is also a consequence of these figures that in order for bursts to occur there must be a pedestal of energy, which is provided by the slow modes. For example, in the neighborhood of $t^+ = 4100$ there is virtually no slow signal [Fig. 11(d)]. Fig. 11(c) shows a substantial fast signal at this time. The net interaction shown in Fig. 11(e) is small and the combined effect as depicted in Fig. 11(b) is relatively feeble. By contrast there is a large pedestal of slow activity centered about $t^+ = 150$ [Fig. 11(d)] but a relatively low level of fast activity [Fig. 11(c)]. The interaction shown in Fig. 11(e) is moderate as is the net effect shown in Fig. 11(b).

Our deliberations up to now lead us to the conclusion that in order for the ejections in Figs. 11(a) and 11(b) to appear both slow (degenerate) and fast (propagating) excitation must be present. As the figures and above discussion have demonstrated one set of modes without the other leads to relatively weak activity. It is natural at this point of the discussion to look into the question of cause and effect and in particular whether the slow modes generate the fast modes or vice versa. The evidence from Fig. 11 is that to lowest order the two modes are independent. This follows from disparate time scales that occur in Figs. 11(c) and 11(d), and the absence of any direct mechanism for generating a fast time scale from a slow one and vice versa.

We also want to assert that the fast modes act as a triggering mechanism for the burst, but these ensue only when there is latent in the flow a pedestal of energy in the slow modes. The issue of using the term *trigger* is partly semantic, and is based on several observations.

First, the propagating modes themselves possess little energy (in fact only 24% of the energy as represented by the first 38 modes). Second, as mentioned above bursting can only occur if fast (propagating) modes are present. Third, the burst shows the same fast activity that is seen in the fast modes. The assertion that the propagating modes are the triggers of bursting activity remains a speculation until more evidence, especially experimental, is presented.

As a final remark we note that the dynamical system considered by Aubry *et al.*[46] is based on what we have termed the kinematically degenerate modes. In fact their system is based on $q = 1$ and $k_1 = 0$, using only the first five spanwise modes, k_3. These authors produce a form of bursting and ejection, which are of a different nature than the structures we have been discussing. Clearly this is an area which needs further investigation.

V. DISCUSSION

An important point to discuss is how representative is our simulation and results of actual turbulence. With this in mind we have examined the channel flow simulations of Moin and Moser[45] and Handler *et al.*[47] In the former case $\mathrm{Re}_\tau = 180$ and in the latter $\mathrm{Re}_\tau = 125$. In both these cases the distribution of energy into what we have termed kinematically degenerate and propagating modes is in rough agreement. Differences in mode ordering can be attributed to variations in computational cell sizes and Reynolds number. It is somewhat difficult to pin down the roll size in a computation. The roll solution shown in Fig. 10 is 200 wall units wide, corresponding to a single pair of rolls. However, as observed in Sec. III, Table I indicates that modes with two and three pairs of rolls also have comparable energies of motion. If the latter case is taken as a basis we see that $200/3 \approx 66$ wall units is also a realistic estimate. This order of magnitude estimate also agrees with the cited works. Also we have confirmed that propagating modes appear in the simulation with $\mathrm{Re}_\tau = 125$.[48]

We can try to make contact with the turbulent spot construction of Henningson. As a first observation we point out that he finds spot growth in an otherwise supercritical steady flow is due to waves that propagate at $\pm 68°$. We find that the most energetic plane waves propagate at the angles $\pm 71.5°$. In view of significant differences in resolution and the nature of the flows the agreement is more than one might hope for. Henningson's construction is based on propagating modes and his primary interest is in describing the growth of a spot in a neighborhood of its boundary.

In a summary, a Karhunen–Loève analysis of low Reynolds number turbulent channel flow has produced empirical eigenfunctions, a subset of which has the form of ob-

liquely propagating plane waves. These waves form an envelope that travels at the velocity corresponding to the location where the Reynolds shear stress is a maximum. The empirical eigenfunction decomposition, unlike the Chebyshev–Fourier decomposition of the direct numerical simulation, is able to extract the regions of main support for these waves; namely, the region near $y^+ = 30$ where the Reynolds stress is a maximum.

The action of these propagating modes, which contain relatively little energy compared to the nonpropagating, or kinematically degenerate modes, may be something akin to a trigger, which can focus on a pedestal of disturbance energy and initiate a bursting or sweeping event. Qualitative support for this idea has been presented. Further work is underway to correlate and quantify these effects, and to extend our analysis in a parametric study with Reynolds number.

ACKNOWLEDGMENTS

We are grateful to B. Knight, R. Moser, R. Handler, and K. Breuer for helpful comments and information. The authors also gratefully acknowledge the use of the Pittsburgh Supercomputing Center.

The work reported here was supported by DARPA-URI N00014-86-K0754.

[1] R. Betchov, Phys. Fluids **3**, 1020 (1960).
[2] P. S. Klebanoff, K. D. Tidstrom and L. H. Sargent, J. Fluid Mech. **12**, 1 (1962).
[3] M. T. Landahl, J. Fluid Mech. **56**, 775 (1972).
[4] S. A. Orszag and A. T. Patera, J. Fluid Mech. **128**, 347 (1983).
[5] S. A. Orszag and A. T. Patera, Phys. Rev. Lett. **45**, 989 (1980).
[6] S. A. Orszag and A. T. Patera, in *Transition and Turbulence*, edited by R. E. Meyer (Academic, New York, 1981), p. 127.
[7] T. Herbert, Bull. Am. Phys. Soc. **26**, 1257 (1981).
[8] T. Herbert, Phys. Fluids **26**, 871 (1983).
[9] T. Herbert, Annu. Rev. Fluid Mech. **20**, 487 (1988).
[10] B. J. Bayley, S. A. Orszag, and T. Herbert, Annu. Rev. Fluid Mech. **20**, 359 (1988).
[11] L. Keefe, P. Moin, and J. Kim, Bull. Am. Phys. Soc. **32**, 2026 (1989).
[12] J. L. Lumley, *Stochastic Tools in Turbulence* (Academic, New York, 1970).
[13] J. L. Lumley, in *Atmospheric Turbulence and Radio Wave Propagation*, edited by A. M. Yaglom and V. I. Tatarski (Nauka, Moscow, 1967), p. 166.
[14] K. S. Ball, L. Sirovich, and L. R. Keefe, Int. J. Numer. Methods Fluids (in press).
[15] D. S. Henningson, P. Spalart and J. Kim, Phys. Fluids **30**, 2914 (1987).
[16] V. C. Patel and M. R. Head, J. Fluid Mech. **38**, 81 (1969).
[17] O. Reynolds, Philos. Trans. R. Soc. London **174**, 935 (1883).
[18] I. Wygnanski, J. Fluid Mech. **59**, 28 (1972).
[19] I. Wygnanski, J. Fluid Mech. **69**, 283 (1975).
[20] P. Bandyopadhyay, J. Fluid Mech. **163**, 439 (1986).
[21] K. S. Breuer, to appear in J. Fluid Mech.
[22] D. R. Carlson, S. E. Widnall, and M. F. Peeters, J. Fluid Mech. **121**, 487 (1982).
[23] D. S. Henningson and P. H. Alfredsson, J. Fluid Mech. **178**, 405 (1987).
[24] D. S. Henningson, Phys. Fluids A **1**, 1876 (1989).
[25] A. L. Kistler and T. Markus, Phys. Fluids A **1**, 1883 (1989).
[26] W. W. Wilmarth, Adv. Appl. Mech. **15**, 197 (1975).
[27] W. W. Wilmarth, Annu. Rev. Fluid Mech. **7**, 13 (1975).
[28] H. T. Kim, S. J. Kline, and W. C. Reynolds, J. Fluid Mech. **50**, 133 (1971).
[29] J. Kim, P. Moin, and R. Moser, J. Fluid Mech. **177**, 133 (1987).
[30] H. Eckelmann, J. Fluid Mech. **65**, 439 (1974).
[31] L. S. Gresko, MIT FDRL Report No. 88-2, 1988.
[32] K. Breuer, to appear in Phys. Fluids A.
[33] R. L. Panton, J. Fluids Eng. (in press).
[34] K. R. Sreenivasan, in *Frontiers in Experimental Fluid Mechanics* (Springer, Berlin, 1989).
[35] A. A. Townsend, J. Fluid Mech. **11**, 97 (1961).
[36] P. Bradshaw, J. Fluid Mech. **30**, 241 (1967).
[37] S. J. Kline, W. C. Reynolds, F. A. Schaub, and P. W. Rundstadler, J. Fluid Mech. **30**, 741 (1967).
[38] A. V. Johansson, P. H. Alfredsson, and J. Kim, in *Proceedings of the* 1987 *Summer Program* (NASA/Stanford Center for Turbulence Research, Stanford, CA, 1987), p. 237.
[39] L. Sirovich, Q. Appl. Math. **45**, 561 (1987).
[40] L. Sirovich and D. Rodriguez, Phys. Lett. A **120**, 211 (1987).
[41] L. Sirovich, Physica D **37**, 126 (1989).
[42] L. Sirovich and M. Kirby, J. Opt. Soc. Am. A **4**, 519 (1987).
[43] L. Sirovich, M. Maxey, and H. Tarman, in *Turbulent Shear Flows 6*, edited by J.-C. Andre *et al.* (Springer, New York, 1989), p. 68.
[44] R. Courant and D. Hilbert, *Methods of Mathematical Physics* (Interscience, New York, 1953), Vol. 2.
[45] P. Moin and R. D. Moser, J. Fluid Mech. **200**, 471 (1988).
[46] N. Aubry, P. Holmes, J. L. Lumley, and E. Stone, J. Fluid Mech. **192**, 115 (1988).
[47] R. A. Handler, E. W. Hendricks, and R. I. Leighton, Naval Research Laboratory Memorandum Report No. 6410 (1989).
[48] K. S. Ball, R. A. Handler, and L. Sirovich, *Twelfth Symposium on Turbulence* (University of Missouri–Rolla, Rolla, MO, 1990), preprint volume, p. B-9.